METRICA
METRology Institutional CAtalog

ISTITUTO NAZIONALE DI RICERCA METROLOGICA
Repository Istituzionale

European partnership in metrology project: Dissemination of the redefined kelvin (DireK-T)

Original
European partnership in metrology project: Dissemination of the redefined kelvin (DireK-T) / Machin, G., Gavioso, R., Dobre, M., Gaiser, C., Martin, M., Underwood, R.. - In: MEASUREMENT. SENSORS. - ISSN 2665-9174. - 38:(2025). [10.1016/j.measen.2024.101620]

Availability:
This version is available at: 11696/87959 since: 2026-02-20T17:01:30Z

Publisher:
Elsevier Ltd

Published
DOI:10.1016/j.measen.2024.101620

Terms of use:

This article is made available under terms and conditions as specified in the corresponding bibliographic description in the repository

Publisher copyright

(Article begins on next page)

15 November 2026

Very-Low-Field MRI Scanners: From the Ideal to the Real Permanent Magnet Array

Umberto Zanovello, Alessandro Arduino, Vittorio Basso, Luca Zilberti, Alessandro Sola, Andrea Agosto, Luca Toso, and Oriano Bottauscio

***Abstract*—Very-low-field (VLF) magnetic resonance imaging (MRI) is becoming increasingly popular due to its portability and adaptability to different environments. They are being successfully used for various clinical applications, leading to a paradigm shift in the way imaging care is typically performed. The development of low-cost MRI scanner prototypes began a few years ago, with some interesting and promising open-source projects emerging in both hardware and software design. Using permanent magnets (PMs) to generate the static magnetic field B_0 can substantially reduce the manufacturing cost while achieving satisfactory homogeneity. This article aims to explore the reasons behind discrepancies between magnet design and prototype performance in terms of magnetic field homogeneity. Understanding the impact of the practical implementation of magnet design could inform the development of more tolerant designs in the future, simplifying subsequent B_0 shimming procedures or even making them unnecessary. This work also evidences the impact of using different numerical model approximations in the modeling phase, proving how they also impact the quality of the design outcomes.**

***Index Terms*—Biomedical equipment, low-field (LF) magnetic resonance imaging (MRI), permanent magnets (PMs), portable MRI, sustainable MRI.**

I. Introduction

MAGNETIC resonance imaging (MRI) technology is developing in two different directions. Ultrahigh-field MRI scanners allow for enhanced image resolution, improved signal-to-noise ratio (SNR), and better contrast than conventional MRI scanners. Conversely, "low-field (LF)" MRI, whose technological evolution is summarized in [1], is becoming increasingly popular due to its portability, affordability, safety, and adaptability to different environments [1], [2]. The use of artificial intelligence (AI) for image reconstruction, combined with properly characterized hardware, has contributed to the growing interest in these solutions, as evidenced by the extensive literature on the subject published in recent years [2], [3], [4], [5], [6], [7], [8]. The attention paid to "LF" MRI led to the organization of the first ISMRM Workshop on Low-Field MRI in 2022 [9].

"LF" MRI are conventionally classified [2], [10] as LF (<0.5 T), very-LF (VLF, 10/100 mT) and ultralow-field (ULF, <10 mT) scanners.

Recently, "LF" scanners have been successfully employed in various clinical applications, including the diagnosis of brain tumors and stroke [11], neuroimaging [12], the evaluation of Alzheimer's disease [13], and dental imaging [14]. Moreover, their portability introduces a point-of-care model, leading to a paradigm shift in the way imaging care is typically performed [15], [16], [17], [18], [19].

Despite being more affordable than their high-field counterparts, proprietary "LF" scanners are still relatively expensive, limiting their use in low- and middle-income countries. The development of low-cost MRI scanner prototypes began a few years ago with some interesting and promising open-source projects involving both hardware and software design. Recent results have shown image quality comparable to that of commercially available scanners [20], [21], [22].

Although adopting permanent magnets (PMs) to generate the static magnetic field (B_0) can substantially reduce the manufacturing cost [23], [24], [25], [26], achieving satisfactory magnetic field homogeneity can be challenging due to the finite diameter-to-length ratio of Halbach arrays and the use of a limited number of PMs. Field inhomogeneity decreases the SNR and causes image distortion when using fast Fourier transform (FFT)-based reconstructions, thus affecting overall image quality [27], [28].

Design optimizations [23], [29], [30], [31], [32] and flexible passive/active shimming approaches [33] are paramount in getting field homogeneity. A recent review [24] provides a compilation of relevant concepts in designing Halbach multipoles for magnetic resonance applications.

Besides achieving satisfactory magnetic field homogeneity, proper design of the different MR hardware proves to be essential for producing high-quality images [34]. Among them, for example, are the design of the radio frequency coil to compensate for the low SNR [35], the design of the gradient coils to minimize distortion caused by ferromagnetic structures [36], and the use of acquisition techniques based on AI tools [37].

Proper metrological characterization of the scanner components is a valuable step in hardware development, providing fundamental information in solving potential issues during

Received 18 July 2025; revised 3 November 2025; accepted 13 November 2025. Date of publication 28 November 2025; date of current version 23 December 2025. This work was supported in part by European Partnership on Metrology, co-financed by European Union's Horizon Europe Research and Innovation Program through the 22HLT02 A4IM Project; and in part by the Participating States. The Associate Editor coordinating the review process was Dr. Rui Yang. *(Corresponding author: Oriano Bottauscio.)*

The authors are with the Istituto Nazionale di Ricerca Metrologica, 10135 Turin, Italy (e-mail: u.zanovello@inrim.it; a.arduino@inrim.it; v.basso@inrim.it; l.zilberti@inrim.it; a.sola@inrim.it; a.agosto@inrim.it; l.toso@inrim.it; o.bottauscio@inrim.it).

Digital Object Identifier 10.1109/TIM.2025.3638912

© 2025 The Authors. This work is licensed under a Creative Commons Attribution 4.0 License.
For more information, see https://creativecommons.org/licenses/by/4.0/

construction and testing the numerical tools used for system design. The latter is particularly critical when it comes to the main magnet. Manufacturing tolerances and the intrinsic magnetic variability of the PMs, together with their dependence on temperature, can in fact be detrimental to scanner performance.

This article fits this context by focusing on the characterization of magnet performance in terms of magnetic field homogeneity for VLF scanners using PMs. The main objective is to investigate the sensitivity of the magnetic field homogeneity to various factors, exploring the reasons behind discrepancies between the performance of the reference design and the built prototype. Within this scope, the analysis has taken as a reference the VLF magnet designed in the framework of the open-source imaging initiative (OSI^2) [38].

Understanding the impact of the choices made during the construction of the magnet can lead to more effective designs. Furthermore, improving the agreement between actual and expected behaviors of the magnet would simplify the subsequent B_0 shimming procedure, for example, by reducing the number and size of shimming magnets and the number of shimming iterations, or even making the shimming phase unnecessary. In this regard, even if the results of this study refer to a specific VLF magnet implementation, they prove to be relevant and useful to the wider portable MRI community.

An additional aim of this study is to quantify the impact of using different numerical model approximations in the design phase, revisiting concepts that are most frequently used in the design of electrical machinery [39]. In particular, while some assumptions may simplify the numerical model and improve its performance in terms of computational time, this article demonstrates how they also impact the quality of the obtained results.

II. Magnet Array

A. Magnet Array Layout

The OSI^2 v2.1 magnet array, called rotation-optimized magnet (ROMA) [40], was considered for this study. The design of the "ROMA" array was optimized by Leiden University Medical Center, and the mechanical frame has been engineered by the Physikalisch-Technische Bundesanstalt (PTB) in Berlin. For the purpose of the analysis here reported, this magnet has been replicated and characterized at INRiM to compare experimental and simulation outcomes.

In the "ROMA" magnet configuration, the orientation of the individual PMs within the array does not adhere to the Halbach theory or its Mandhala discretization [41]. Instead, the orientation of the PMs is the result of an optimization procedure designed to maximize the magnetic field homogeneity within a 200 mm diameter spherical volume (DSV) at the center of the magnet.

The ROMA array comprises 1936 NdFeB N52 PMs measuring $(12 \times 12 \times 12)$ mm^3, arranged in two circular layers along 16 rings. The rings are made of polypropylene (PP) using a computer numerical control (CNC) milling process.

Two additional rings close the array at the extremities. These rings contain 384 NdFeB N52 PMs measuring $(12 \times 12 \times 50)$ mm^3 arranged on three circular layers. Fig. 1 shows an overview of the entire setup. The bore diameter is 322 mm, with an axial length of 420 mm.

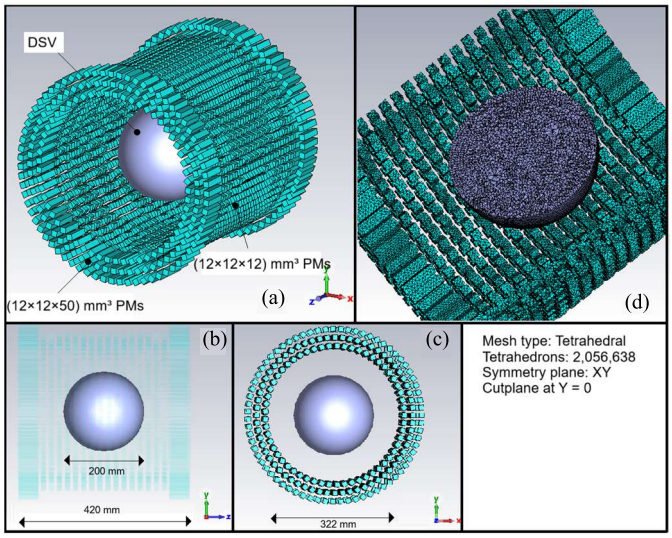

Fig. 1. Magnet array configuration with the considered spherical DSV. (a) 3-D view, (b) lateral view, with total magnet length and DSV diameter size, (c) front view with the bore internal diameter, and (d) finite element mesh adopted in the modeling phase described in Section IV. The magnetic flux density B_0 in the DSV is mainly oriented along the x-axis.

The mass of the magnet array is approximately 100 kg. The target magnetic flux density (B_0) at the isocenter is approximately 50 mT, oriented along the x-axis.

B. PMs Magnetic Characteristics

The magnetic characteristics of the NdFeB PMs used to build the array were measured using the hysteresisgraph method at temperatures ranging from 18 °C to 50 °C.

The following relationships fit the dependence of the residual polarization J_r and magnetic coercivity H_c on temperature T:

$$J_r = J_{r0}\left[1 + K_J\left(T - T_{\text{ref}}\right)\right] \tag{1a}$$

$$H_c = H_{c0}\left[1 + K_{H1}\left(T - T_{\text{ref}}\right) + K_{H2}\left(T - T_{\text{ref}}\right)^2\right] \tag{1b}$$

with J_{r0} (H_{c0}) equal to 1.431 T (–955.3 kA/m) and 1.462 T (–941.2 kA/m) for the $(12 \times 12 \times 12)$ mm^3 and $(50 \times 12 \times 12)$ mm^3 PMs, respectively. T_{ref} is the reference temperature at which J_{r0} and H_{c0} were measured (T_{ref} = 18 °C in our case), K_J = –1.26 10^{-3}°C^{-1}, K_{H1} = –0.01 °C^{-1} and K_{H2} = +3.8 10^{-5}°C^{-2}.

Fig. 2 shows the magnetization curves of $(12 \times 12 \times 12)$ mm^3 and $(12 \times 12 \times 50)$ mm^3 PM samples related to 24 °C. Magnetization curves are shown in terms of magnetic flux density (B) and magnetic polarization (J) versus magnetic field (H). Despite being provided by the same producer, the PMs exhibit some differences in their magnetic characteristics.

III. Experimental Characterization of the Magnet Array

The magnet array was assembled in accordance with the guidelines provided in [42]. Each PM was tested before being

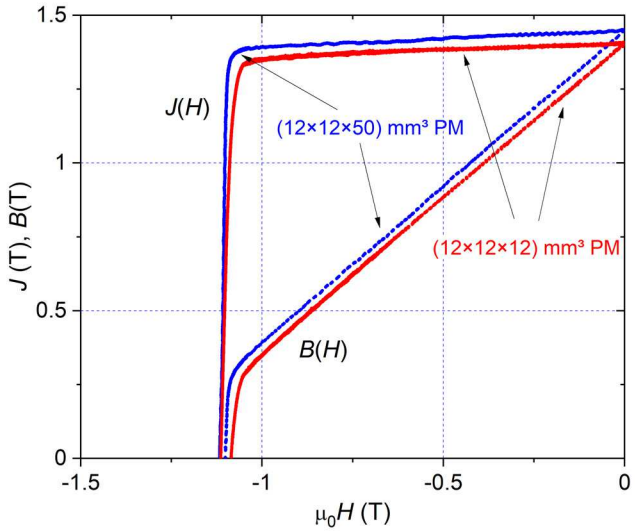

Fig. 2. Magnetic characteristics of the two samples of NdFeB N52 PMs. Curves reported in the figures refer to 24 °C.

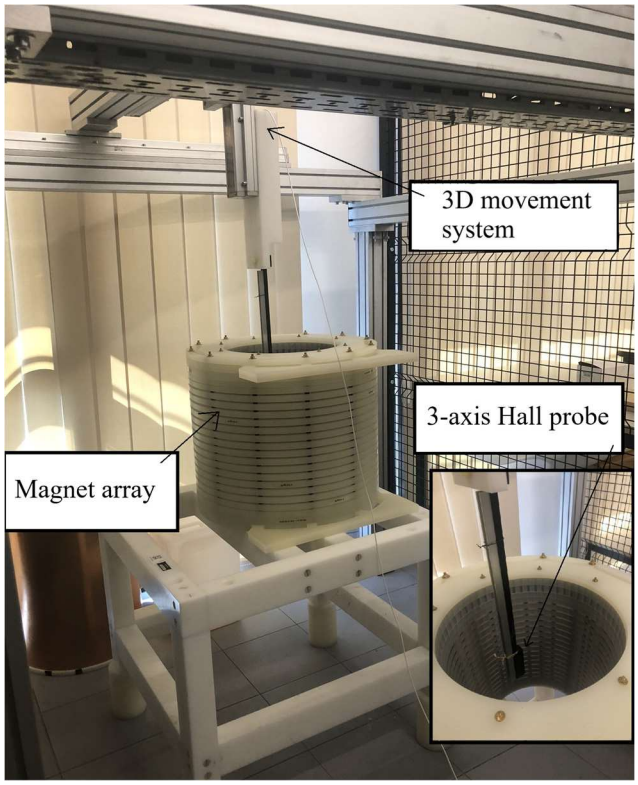

Fig. 3. Photograph of the assembled array placed within the 3-D movement system used to perform the magnetic measurements in the DSV.

inserted in the rings using a properly designed magnet test station [43], [44]. The assembled array was placed in a 3-D automatic movement system, with the z-axis aligned with the vertical axis of the plotter to perform magnetic field measurements in the DSV. Fig. 3 shows a photograph of the array inside the 3-D movement system.

Measurements were performed using a SENIS 3MH6-E teslameter, which has 3-axis Hall probes packed in a volume of $(100 \times 10 \times 100)\ \mu\text{m}^3$ to ensure optimum spatial resolution. The probe was fixed to the movement system using ad hoc support, and a Python program synchronized the movement and acquisition processes. The acquisition pipeline allowed sufficient idle time between consecutive measurements to ensure that probe oscillations due to probe motion were fully damped. Before the acquisition, the magnet array was left in the laboratory for over 24 h. This allowed all the PMs to reach the laboratory temperature of 24 °C ± 2 °C. In addition, the Python software recorded the temperature measured by the sensor integrated within the magnetic field probe for each magnetic field acquisition, resulting in an average temperature of 23.7 °C ± 0.3 °C. This information was used in both the simulation and calculation of the uncertainty budget.

The magnetic field was measured inside the 200 mm DSV in uniformly distributed 4224 points, defined by an equally spaced Cartesian grid with steps equal to 10 mm along the x-, y-, and z-directions. The grid resolution was chosen as a tradeoff between sufficient spatial resolution and elapsed measurement time, considering that the entire acquisition took approximately 10 h to complete. The contribution of the Earth's magnetic field was removed from the measured data.

The field homogeneity of B_x in the DSV was quantified by the following two metrics:

$$\text{DIS}_1 = \frac{\text{Max}\,(B_x) - \text{Min}\,(B_x)}{\text{Mean}\,(B_x)} \tag{2a}$$

$$\text{DIS}_2 = \frac{\text{Std}\,(B_x)}{\text{Mean}\,(B_x)}. \tag{2b}$$

All the statistics (Max, Min, Mean, and Std) were evaluated on the measured sampled values. The use of a uniform grid enables us to compute the mean and standard deviation of the spatial distribution of the magnetic field component B_x in the DSV directly as the sample mean and sample standard deviation of the measured values.

The DIS_1 parameter is widely adopted by the MRI community [14], [20], [31], [41] and facilitates comparison with other implementations. Whereas it shows correlations with image quality in terms of signal intensity and distortions [27], [28], it is based on local values of the B_0 field (maximum and minimum values). The MRI signal is the result of all the signals emitted by the excited magnetization vectors. This consideration justifies the adoption of the integral DIS_2 parameter, which incorporates the effects of all spatial values, as an alternative to DIS_1.

It is worth noting that DIS_2 is controlled by DIS_1 in the sense that $\text{DIS}_2 \leq \text{DIS}_1$. In particular, the equality is only verified when $\text{DIS}_1 = 0$. Consequently, it is possible to have a small DIS_2 and a large DIS_1, but not vice versa.

The average magnetic flux density measured was 48.056 mT, with a relative uncertainty of 166 ppm. The experimental DIS_1 and DIS_2 values were 24 600 ± 1300 ppm and 4400 ± 1300 ppm, respectively. The expanded uncertainty values (95% level of confidence) were estimated according to the procedure described in Appendix A. The measured DIS_1 value is comparable with the one obtained in other practical realizations of scanners before shimming (see [7], [20]).

IV. Numerical Models

In the simulation environment, the z-axis is oriented along the bore axis, with the main component of the static magnetic field oriented along the x-axis (see Fig. 1). The magnetic field homogeneity was theoretically evaluated in the 200 mm DSV by adopting two different modeling approaches: the finite element method (FEM) and the dipole model. These approaches were further specialized in the way they dealt with the nonlinear magnetic characteristics of the PMs. The FEM approach is more computationally demanding but provides a more reliable solution for the actual PM geometry. The dipole model enables faster calculations by using closed-form approximations to compute the magnetic field generated by the PMs.

A. Finite Element Solver

Due to its better geometrical accuracy, the FEM solution was used as a reference for validating the dipole models. The geometric configuration of the magnet array was imported into CST Studio Suite [45]. A bounding box with sides of 1 m was set around the magnet array with open boundary conditions. A symmetry constraint was imposed on the xy plane at $z = 0$, and the structure was then discretized into conformal tetrahedral elements. A magnetostatic solver with mesh adaptation was then used. The solver accuracy was set to 10^{-9}, resulting in 2.1×10^6 tetrahedra after mesh refinement. The average mesh quality (ratio between inradius and circumradius) was 0.71, with a minimum and maximum edge lengths of 0.78 mm (close to the PMs) and 100 mm (toward the external boundaries). Fig. 1(d) provides a view of the mesh.

The solver modeled the PM characteristics with two different levels of approximation.

1) Linear magnetic characteristics extrapolated from the data in Fig. 2 around the remanence point, as

$$B = \mu_0 H + J = \mu_0 H + \mu_0 \mu_M H + J_r \tag{3}$$

where μ_M is equal to 0.0223 and 0.0168, for the $(12 \times 12 \times 12)$ and $(50 \times 12 \times 12)$ mm^3 PMs, respectively, μ_0 is the magnetic permeability of vacuum, and J_r was assumed to be equal to the value obtained by (1a) at the working temperature.

2) Nonlinear behavior deduced from the measurements.

B. Dipole Model

The dipole solver is based on the work of Engel-Herbert and Hesjedal [46], in which the authors propose an analytical solution for the magnetic field produced by a bar-shaped PM under the assumption of uniform magnetization. A local Cartesian coordinate system (u, v, w) with associated unit vectors (u, v, w) is centered on the barycenter of the magnet bar, having dimensions ($2L_u$, $2L_v$, $2L_w$). Being the local v-axis oriented along the magnetization J_v, the analytical expressions for the magnetic field components H at a generic point (u, v, w) are given by, as shown at the bottom of the next page, The above equations represent the "external" magnetic field generated by a given PM within the surrounding volume. They can be summarized in vector form as follows:

$$\boldsymbol{H}_{\text{ext}} = \begin{pmatrix} H_{u,\text{ext}} \\ H_{v,\text{ext}} \\ H_{w,\text{ext}} \end{pmatrix} = J_v \begin{pmatrix} f_u \\ f_v \\ f_w \end{pmatrix} = J_v \boldsymbol{F}. \tag{5}$$

$\boldsymbol{F}$ is a column array whose elements are derived from (B4).

Similar to FEM, the dipole model was extended to account for the interaction between the surrounding magnets, modeling both the linear and nonlinear characteristics of the NdFeB N52 magnetization curve. Details about the dipole model extensions are reported in Appendix B, together with a simple diagram showing how FEM and dipole models approximate the PMs array.

TABLE I

Measured and Simulated Values of the Mean Value of B_x in the DSV and Field Homogeneity With the Two Adopted Metrics (DIS_1 and DIS_2). The Values Correspond to the PM Characteristic at 23.7 °C. In the Experiments, the Expanded Uncertainty (with 95% level of confidence), Estimated as Described in Appendix A, Is Reported. Both FEM and Dipole Simulations Are Reported

Case	*Mean*(B_x) (mT)	DIS_1 (ppm)	DIS_2 (ppm)	Total computational time (*) (hh:mm:ss)
Experiments	48.056 ± 0.008	24600 ± 1300	4400 ± 1300	-
Ideal Dipole	48.938	266	26.4	00:00:15
Dipole with reaction linear *H-J* curve	48.581	1180	209	00:00:29
FEM with linear *H-J* curve	48.205	1246	184	00:34:00
Dipole with reaction nonlinear *H-J* curve	47.908	1720	316	00:01:07
FEM with nonlinear *H-J* curve	47.905	2165	394	01:24:00

Note: (*) They include all computational phases (pre-processing, solver and post-processing).

C. Dipole Approach Versus Finite Element Results

The dipole approach was validated against FEM, considering the data of the ROMA array configuration published in [40]. To comply with the assumptions of the optimization procedure that led to the magnet design, all simulations assumed the same magnetic characteristics for all the PMs equal to those of the $(12 \times 12 \times 12)$ mm^3 PMs. The results were compared in terms of the relative discrepancy in the $L2$-norm of the x-component of the magnetic flux density (B_x), sampled in the same N points ($N = 4224$) mapped in the experiments. Simulations were performed with PMs characteristic at 23.7 °C, allowing comparison with experiments

$$L2 - \text{norm} = \sum_i^N \left(B_{x,\text{dipole}}^{(i)} - B_{x,\text{CST}}^{(i)} \right)^2 \Big/ \sum_i^N \left(B_{x,\text{CST}}^{(i)} \right)^2. \tag{6}$$

In (B4) $B_{x,\text{dipole}}^{(i)}$ and $B_{x,\text{CST}}^{(i)}$ are the values computed by the dipole model and CST, respectively, using either the linear or

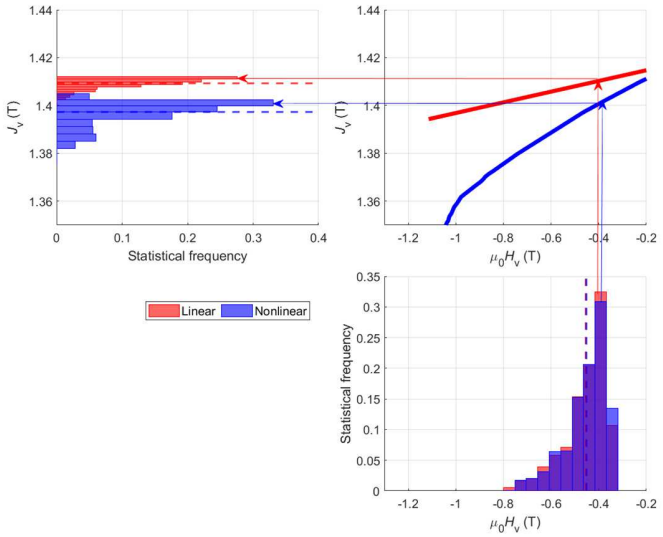

Fig. 4. Statistical distribution of the working point (H_v, J_v) of every single PM using linear and nonlinear PM characteristics. Top left plot: statistical frequency of J_v values, Top right plot: H–J characteristic of the PMs, Bottom right plot: statistical frequency of H_v values. The dashed lines are the mean values of J_v and H_v. The arrows illustrate the correspondence between H_v and J_v values within a single magnet for the linear and nonlinear cases.

nonlinear solver. The relative discrepancies are 4.67×10^{-7} and 3.22×10^{-6} for the linear and nonlinear cases, respectively, indicating good agreement between the two modeling approaches.

Table I summarizes experimental and computed results with increasing level of complexity, starting from the ideal dipole approximation, i.e., when the dipoles are assumed to have a working point corresponding to a magnetic polarization equal to J_r. This latter approach produces results that are inconsistent with those obtained using FEM.

The differences between the results obtained by assuming linear and nonlinear PM characteristics can be explained by the different working points of each PM, which result from their interaction. The plots in Fig. 4 show the distribution of the magnetic field (H_v) and polarization (J_v) components in each PM for the two cases. While the H_v distributions are similar, the J_v distributions differ significantly, with a lower mean value for the nonlinear case.

Table I also summarizes the computational times required for the different modeling approaches. The FEM results were obtained using the magnetostatic CST solver (CST Studio Suite 2025), while the dipole results were obtained using a custom-made MATLAB R2022a script [47]. The computational times refer to the solutions obtained using an Intel[1] Xeon[1] Gold 6430 processor with a frequency of 2.10 GHz and 512 GB of RAM.

With the exception of the FEM model, the computational time scales almost linearly with the number of computational points in the DSV. For FEM, the computational time is related to the mesh size of the entire domain. In any case, the burden on the measurement process definitely overcomes one of the computations.

Based on these outcomes, the dipole model was found to be accurate enough for all subsequent analyses. It also considerably reduced the computational burden, enabling Monte Carlo (MC) analyses that would not have been feasible with FEM.

V. Deviations Between the Prototype and Reference Design

Despite the great care taken in manufacturing the magnet components and assembling the final array, the comparison between measurements and simulations revealed significant discrepancies in terms of field homogeneity. This section investigates several possible deviations from the ideal structure and their impact on field homogeneity.

We drew up an inventory of the main reasons for deviation based on building, design, and manufacturing experience. They can be either deterministic or stochastic in nature. Both cause the array to behave differently from the reference design, but whereas the former can be accurately determined and possibly

[1]Registeredtrademark.

$$H_u(u,v,w) = \mu_0 \frac{J_v}{4\pi} \sum_{k,l,m=1}^{2} (-1)^{k+l+m} \log\left(w + (-1)^m L_w + \sqrt{\left[u + (-1)^k L_u\right]^2 + \left[v + (-1)^l L_v\right]^2 + \left[w + (-1)^m L_w\right]^2}\right) \tag{4a}$$

$$H_v(u,v,w) = -\mu_0 \frac{J_v}{4\pi} \sum_{k,l,m=1}^{2} (-1)^{k+l+m} \frac{\left[v + (-1)^l L_v\right] \cdot \left[u + (-1)^k L_u\right]}{\left|v + (-1)^l L_v\right| \cdot \left|u + (-1)^k L_u\right|} \times \arctan\left(\frac{\left|u + (-1)^k L_u\right| \cdot \left[w + (-1)^m L_w\right]}{\left|v + (-1)^l L_v\right| \cdot \sqrt{\left[u + (-1)^k L_u\right]^2 + \left[v + (-1)^l L_v\right]^2 + \left[w + (-1)^m L_w\right]^2}}\right) \tag{4b}$$

$$H_w(u,v,w) = \mu_0 \frac{J_v}{4\pi} \sum_{k,l,m=1}^{2} (-1)^{k+l+m} \log\left(u + (-1)^k L_u + \sqrt{\left[u + (-1)^k L_u\right]^2 + \left[v + (-1)^l L_v\right]^2 + \left[w + (-1)^m L_w\right]^2}\right). \tag{4c}$$

corrected in a new design, the latter can only be compensated for through shimming strategies.

In Sections V-A and V-B, these two sources of deviation are investigated in detail. Equation (1) was applied to perform simulations at an average temperature of 23.7 °C, as measured during the experiments.

A. Deterministic Causes of Deviation

Three possible deterministic causes of deviation from design to prototypes have been identified: 1) the different magnetic characteristics of the two PM types; 2) the ring positioning along the z-axis; and 3) the modification of PM orientations due to mechanical forces. These three causes were studied in strict sequence, with each subsequent effect evaluated on top of the previous one.

All of them have a deterministic character, because they can be quantified and, in principle, compensated during the design phase.

1) Different PM Characteristics: The hysteresisgraph measurements in Section II-B revealed different behavior between the $(12 \times 12 \times 12)$ and $(12 \times 12 \times 50)$ mm^3 PMs, even though they are both N52 type and supplied by the same manufacturer. This significant difference in behavior affects the magnetic field homogeneity due to the unbalanced contribution of the short and long PMs. Considering the different PM characteristics, the values of DIS_1 and DIS_2 increased from 1720 to 6960 ppm and from 316 to 1340 ppm, respectively.

2) Ring Positioning Along Z-Axis: Another cause of deviation from ideal behavior that was investigated is the position of the rings along the z-axis. Indeed, the strong attraction or repulsion between the adjacent rings slightly affects their distance, which cannot be compensated for using the threaded rods to pack the frames. Therefore, the position of each ring was measured using a caliper on the built array. The small deviation of the central position of each ring from the reference design was determined to repeat the computation. This source of deviation has an opposite effect on DIS_1 and DIS_2 values, leading to a small reduction of the values obtained with the previous correction from 6960 to 6520 ppm and from 1340 to 1150 ppm, respectively.

3) Rotation of PM Orientation Due to Mechanical Torque: The small rotations of the PMs with respect to their reference orientation, which are caused by their mechanical interactions, were investigated. These rotations can be estimated by computing the torque acting on each PM because of the interactions with all other PMs. Fig. 5 shows the behavior of the torque acting in the xy plane on every single PM. In the figure, only a selection of rings is shown for brevity. The other torque components, acting on xz and yz planes, are lower (always less than 10%). Therefore, assuming that the mechanical constraints provided by the frame containing the magnets are similar along the three axes of rotation, the effects of such torques are neglected. This choice, which has been subjected to verification a posteriori, is also justified by the fact that the magnetization of the magnets is orthogonal to the z-axis, making rotations in the xy plane more relevant for the correct determination of the field in the DSV.

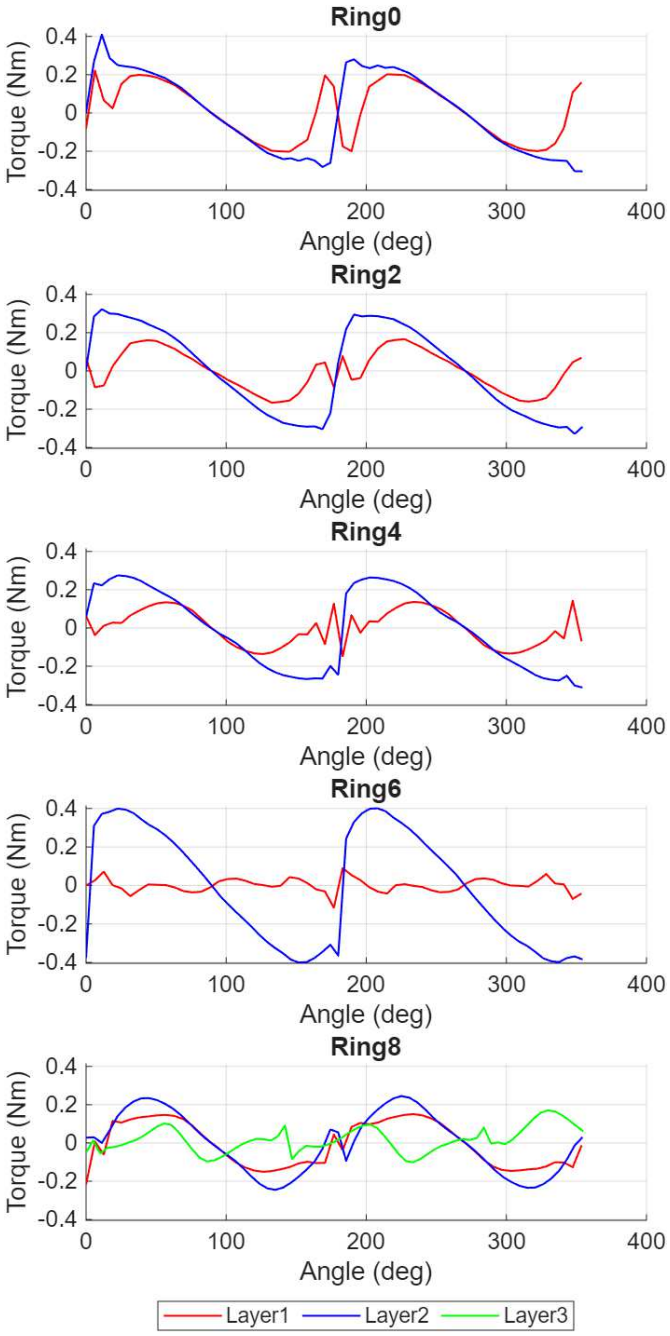

Fig. 5. Behavior of the torque acting in the xy plane on each PM due to the interaction with all other PMs. The figure shows the torque acting on the even rings placed on the positive z-axis [from the one closest to the isocenter (Ring0) and to the one at the extremity (Ring8)]. Lines connecting scattered data are just a guide for the eyes.

PM rotation is a consequence of the backlash within the frame pocket. Its magnitude depends on several factors, some of which are stochastic, such as manufacturing tolerances and variability in PM dimensions, while others depend on design and mechanical requirements. In the realized array, the magnet pockets provided a good fit for the PMs while still allowing easy manual insertion. Due to other difficult-to-account-for influencing factors, deciding upon a reference rotation angle is not an easy task. For example, PP manufacturing is likely to increase CNC tolerance, and the force applied by the PMs

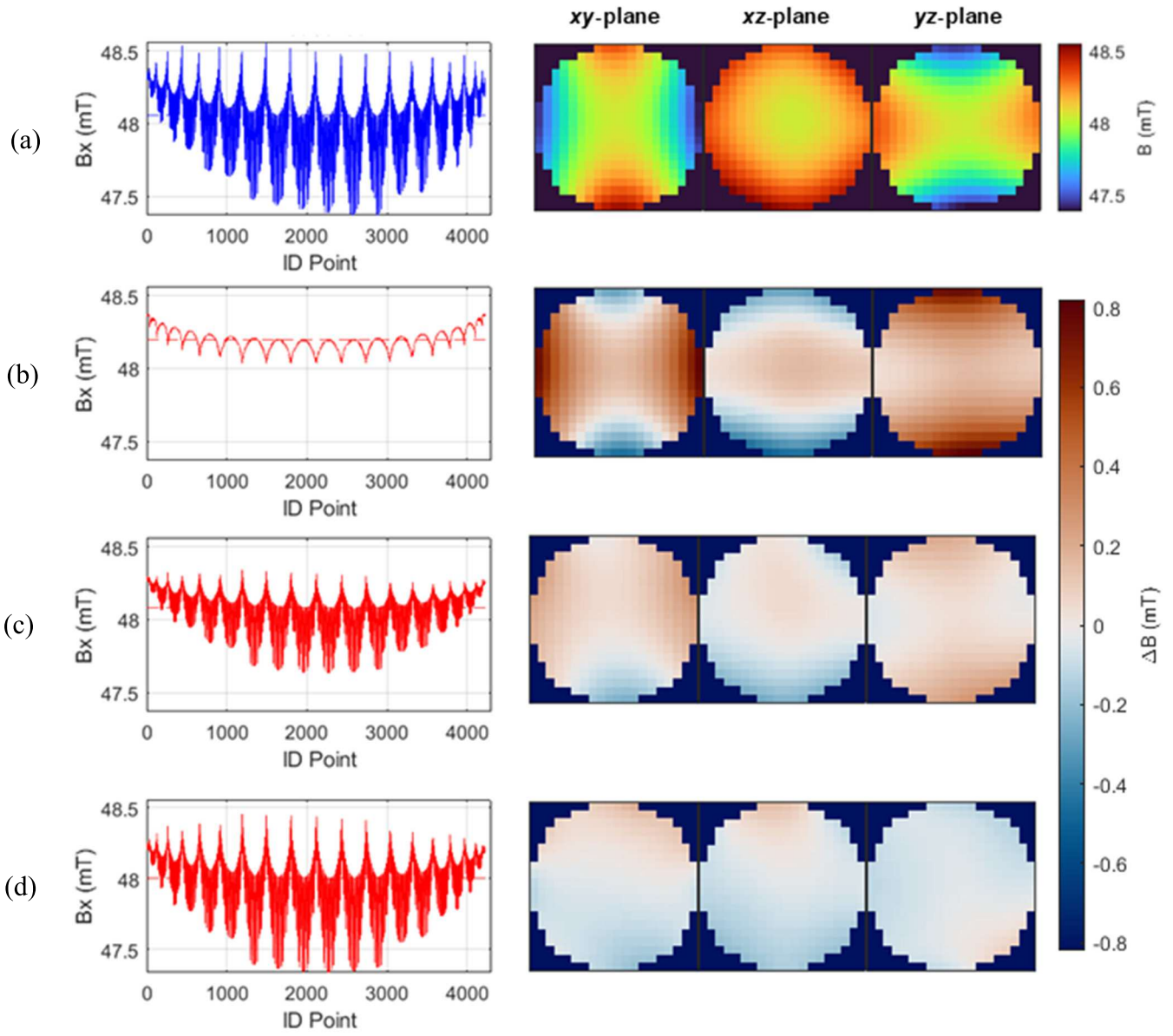

Fig. 6. Comparison between measured and computed B_x values within the DSV. On the left side, the measured and computed values are sampled on the 4224 measurement points. On the right side, the corresponding maps are in the *xy*, *xz*, and *yz* planes. From top to bottom row: (a) measured sampled values and corresponding maps of B_x; from (b) to (d) computed sampled values of B_x and corresponding maps of the difference ΔB with respect to measurements, with (b) PMs having the theoretical orientation, (c) PMs rotated by $\pm 0.8°$, and (d) PMs rotated by $\pm 1.2°$.

to the frame may deform the pockets slightly. Therefore, the investigation considered three values of reasonable rotation angles of the PMs inside their pockets: $\pm 0.8°$, $\pm 1.0°$, and $\pm 1.2°$. These angles correspond to pockets that are 0.13, 0.17, and 0.2 mm larger than the 12 mm side of the PM, respectively.

The amplitude of the rotational angles is applied identically to all PMs without regard for the torque acting on each individual PM. However, the sign of the rotation with respect to the reference orientation is correlated with the sign of the torque acting on each specific PM.

Fig. 6 illustrates the impact of the PM rotations. The plots on the left show the values of B_x sampled on the 4224 measurement points within the DSV. Measured outcomes can be compared with the computed values obtained with the theoretical orientation of PMs and the ones obtained when PMs are rotated by $\pm 0.8°$ or $\pm 1.2°$, according to the sign of the computed torque. These results are obtained by having already included the different PM characteristics and adjustment of the *z*-position of the rings as discussed in Sections V-A1 and V-A2.

We notice that the good agreement between the B_x trends shown in Fig. 6(a) and (d) provides, retrospectively, confirmation of the validity of the choice to consider only the torque components that act in the *xy* plane.

In the same figure, the impact on the spatial distribution of B_x on the *xy*, *xz*, and *yz* planes is also shown. Adjusting the PM rotation, the values of the difference ΔB with respect

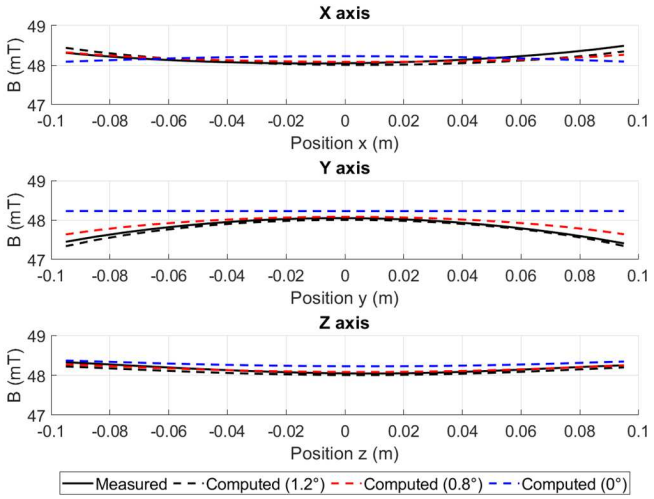

Fig. 7. B_x values along the Cartesian axes in the DSV. The measured values (solid lines) are compared with the computed ones with PMs having the ideal orientation (dashed blue lines), with PMs rotated by $\pm 0.8°$ (dashed red lines), and with PMs rotated by $\pm 1.2°$ (dashed black lines).

to the measurements reduce as proved by the corresponding maps.

Considering all the above-mentioned deterministic causes of variabilities, the values of DIS_1 (resp. DIS_2) were found to be 14 670 ppm (resp. 2670 ppm) for $\pm 0.8°$, 18 930 ppm (resp. 3340 ppm) for $\pm 1.0°$, and 23 200 ppm (resp. 4028 ppm) for $\pm 1.2°$. Despite these being rather small angles, the results reveal the significant impact of this effect on the assembled magnet array. This effect also leads to a good agreement between the measured and simulated B_x field along the Cartesian axes (Fig. 7) and along z-lines outside the DSV (Fig. 8) obtained with the rotational angle of $\pm 1.2°$.

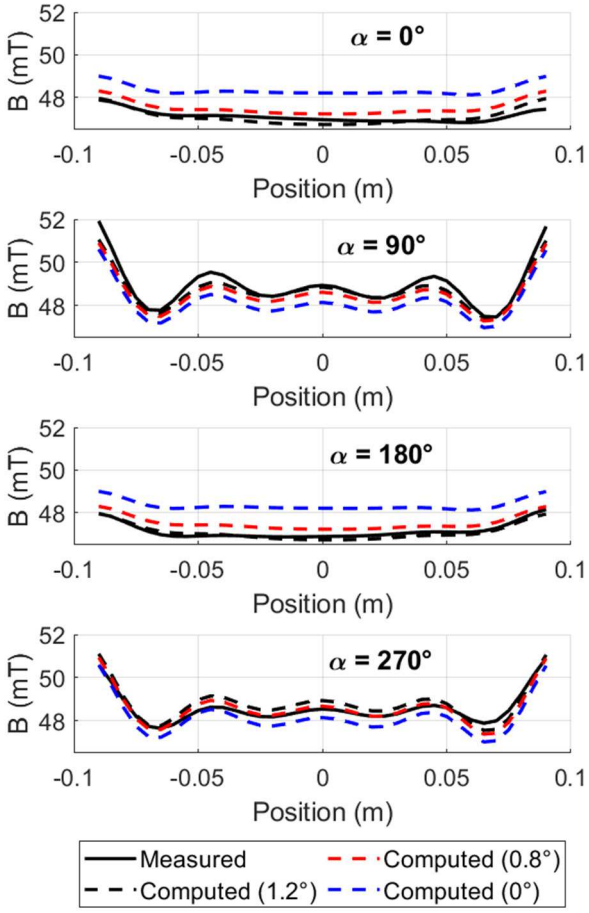

Fig. 8. B_x values along four z-lines (from −0.09 to + 0.09 m) outside the DSV at a radius equal to 0.12 m and spaced by 90° in the xy plane. For each plot α is the angle (in degrees) is with respect to the x-axis. The measured values (solid lines) are compared with the computed ones with PMs having the ideal orientation (dashed blue lines), with PMs rotated by $\pm 0.8°$ (dashed red lines), and with PMs rotated by $\pm 1.2°$ (dashed black lines).

B. Stochastic Causes of Deviation

After including all the deterministic causes of deviation, the following additional stochastic effects were accounted for in the investigations.

1) Variability of the residual polarization of each PM sample.
2) Measurement uncertainty in the characterization of the PM nonlinear characteristics.
3) Uncertainty in each PM rotation.
4) PM positioning due to dimensional tolerances in the CNC machinery used to produce the PP rings.

Unlike the deterministic causes of deviation analyzed in Section V-A, these effects cannot be compensated for during the design phase. However, they can be used to assign an uncertainty value to the design prediction.

These effects were all studied separately to quantify their impact, and they were applied on top of the deterministic effects identified in Section V-A, i.e., the different PM characteristics, the adjustment of the z-position of the rings, and the rotational angles of $\pm 1.2°$ of the PM due to the torque.

The analysis assumed a statistical distribution of the input quantities based on measurements or assumptions. MC simulations were then performed to determine the statistical distribution of the output quantities (i.e., the mean value of B_x in the DSV and the DIS_1 and DIS_2 values). For each simulation, the input quantity was randomly extracted from its statistical distribution. The MC analysis was based on 1000 extractions. The stability of the MC outcomes versus the number of extractions was verified a posteriori, with the output deviation remaining below 0.3% when increasing the number of extractions to 10 000.

All results are collected in Table II, which shows the expected values, expanded uncertainty with a level of confidence of 95% of Mean(B_x), DIS_1, and DIS_2 in the DSV.

1) Variability of the Residual Polarization of PMs: Although the magnetic remanence of the PMs is a specification provided by the manufacturer and measured by the hysteresisgraph on a selected sample, the actual value of each PM may differ slightly due to manufacturing and magnetization processes, storage conditions, etc. As a hysteresisgraph measurement takes a long time, it was not feasible to perform a complete magnetic characterization of all PMs. Therefore, the dispersion of the magnetic remanence of 20 samples randomly extracted from the $(12 \times 12 \times 12)$ mm^3 batch and ten samples from the $(12 \times 12 \times 50)$ mm^3 batch was estimated by

TABLE II

RESULTS OF THE STOCHASTIC SIMULATIONS. FOR EACH INPUT VARIABILITY, THE TABLE COLLECTS THE EXPECTED VALUES AND EXPANDED UNCERTAINTIES (WITH A 95% LEVEL OF CONFIDENCE) OF MEAN(B_x), DIS_1, AND DIS_2

Input variability	$Mean(B_x)$ (mT)	DIS_1 (ppm)	DIS_2 (ppm)
PMs residual polarization	48.01 ± 0.008	23300 ± 878	4030 ± 92
Measurement uncertainty in PM magnetic characterization	48.01 ± 0.58	23400 ± 1726	4080 ± 221
Uncertainty in PM orientation	48.00 ± 0.010	23370 ± 757	4032 ± 90
Uncertainty in PM positioning	48.00 ± 0.004	23260 ± 481	4029 ± 46
Combination of all variabilities	48.00 ± 0.55	23600 ± 2034	4100 ± 266
Experiments	48.056 ± 0.008	24600 ± 1300	4400 ± 1300

characterizing their working point. The magnetic moment was measured using the extraction method [48], and the relative standard deviations of the two distributions were found to be 0.59% and 0.26%, respectively.

MC simulations were performed by randomly extracting the value of $J_r^{(i)}$ for each PM from a Gaussian distribution with a mean value (resp., standard deviation) of 1.421 T (8.2 mT) for the $(12 \times 12 \times 12)$ mm^3 PMs and 1.451 T (3.8 mT) for the $(12 \times 12 \times 50)$ mm^3 PMs.

2) Measurement Uncertainty in Pm Magnetic Characterization: An expanded measurement uncertainty (95% coverage interval) of 1.5% is associated with the hysteresisgraph measurement procedure adopted in INRiM laboratories [49]. Therefore, a multiplicative correction coefficient for the PM magnetization characteristics was randomly extracted from a Gaussian statistical distribution having a mean value equal to 1 and a standard deviation equal to 0.0075.

3) Uncertainty in PM Orientation: The stochastic analysis applied an additional rotation angle on top of the 1.2° deterministic one. The value of this angle was extracted from a uniform distribution having bounds equal to 0.68° and 1.72°. These values are a consequence of the dimensional tolerances of sintered NdFeB PMs (±0.05 mm [50]), and the H10 mechanical tolerance recommended for CNC production of the PP rings [51]. The lower and upper bounds are obtained with the smallest pocket and largest PM, and with the largest pocket and smallest PM, respectively.

4) Uncertainty in PM Positioning: In Section V-B3, we accepted that the pockets could be up to 0.235 mm larger than the actual dimensions of the PMs to motivate a ±1.72° rotation of the PMs inside their pockets. Considering a dimension of the PM decreased by its 0.05 mm tolerance, the position of each PM can vary within a range of ±0.14 mm in the plane. These values were used as lower and upper limits of a uniform statistical distribution of the PM position deviation in the MC simulations.

5) Combination of All Stochastic Variabilities: Finally, an MC simulation was performed, accounting for all of the above sources of variability that were assumed to be uncorrelated.

TABLE III

COLLECTION OF ALL THE UNCERTAINTY CONTRIBUTIONS OF THE B_X, DIS_1, AND DIS_2 MEASURED VALUES. $u(x)$ AND $U(x)$ ARE THE STANDARD AND EXPANDED UNCERTAINTY VALUES, RESPECTIVELY. K IS THE COVERAGE FACTOR AND PDF IS THE PROBABILITY DENSITY FUNCTION. THE UNCERTAINTY CONTRIBUTION WAS LINEARLY PROPAGATED TO THE DIS_1 AND DIS_2 VALUES AND ARE REPORTED IN THE LAST TWO ROWS

	Best Estimate	$u(x)$	K	$U(x)$	PDF
$B_{x,meas}$	$B_{x,meas,i}$	$50\ 10^{-6} \cdot B_{x,meas,i}$	2	$100\ 10^{-6} \cdot B_{x,meas,i}$	Normal
C_{noise}	0	< 1 μT	2	< 1 μT	Normal
C_{res}	0	< 1 μT	0.95√3	< 1 μT	Uniform
C_{avg}	0	< 1 μT	0.95√3	< 1 μT	Uniform
C_{pos}	0	3.9 μT	0.95√3	6.4 μT	Uniform
C_{temp}	0	$406\ 10^{-6} \cdot B_{x,meas,i}$	0.95√3	$668\ 10^{-6} \cdot B_{x,meas,i}$	Uniform
$C_{off,1}$	1	$0.014 \cdot DIS_1$	0.95√3	$0.023 \cdot DIS_1$	Uniform
$C_{off,2}$	1	$0.003 \cdot DIS_2$	0.95√3	$0.005 \cdot DIS_2$	Uniform
DIS_1	24638 ppm	642 ppm	2	1283 ppm	Normal
DIS_2	4353 ppm	643 ppm	2	1286 ppm	Normal

VI. DISCUSSIONS

The three deterministic causes of discrepancies between the homogeneity of the design outcomes and the prototype measurements have different impacts. They were studied in strict sequence, leading to variation in DIS_1 (resp. DIS_2) from the design values of 1720 ppm (316 ppm) to 6960 ppm (1340 ppm) (different PM characteristics), to 6520 ppm (1150 ppm) (ring positioning), and to 23 200 ppm (4028 ppm) (max PM orientation due to torque). Corresponding relative variations are: + 4.05 (+ 4.24), –0.94 (–0.86), and + 3.56 (+ 3.50), respectively. The relative variations evidence the significant effect of both using different PM types in the array and the variation of PM orientation due to mechanical forces. Conversely, the deviation of the ring positions along the z-axis with respect to their reference values only causes relatively low effects.

This observation has a direct consequence for magnet designs. For example, the adoption of different PM types should be avoided if possible. Even when the PMs are of the same type (e.g., N52 in our example), their magnetic characteristics could slightly differ, introducing a potential cause of variability between the ideal prediction and the final realization.

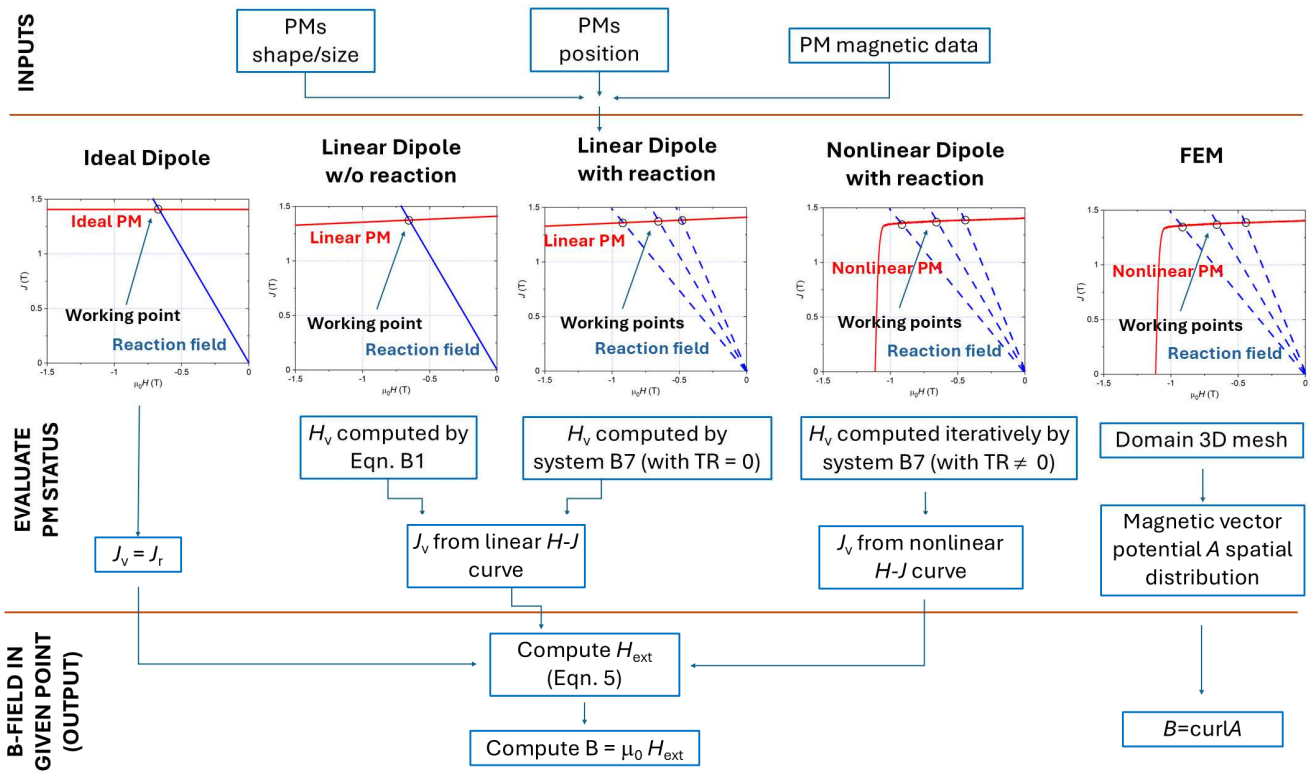

Fig. 9. Schematic showing the different ways of modeling the PMs array.

The modification of PM orientation due to forces could be properly considered during the magnet optimization, either by reducing the likelihood of magnet rotation or by milling the magnet pockets at a slight angle in the opposite direction to compensate for it. This result also directly affects the choice of manufacturing tolerances, particularly in ring production.

Rather than providing strategies for compensation during the design phase, the analysis of potential stochastic effects allowed us to assign an uncertainty value to the design prediction.

The most significant stochastic effect was attributed to the measurement uncertainty in PM magnetic characterization. This effect introduces a bias in the expected value of DIS_1 of + 0.9% (23 400 ppm instead of 23 200 ppm) with a relative expanded uncertainty of ±7.3% (95% coverage interval). At the same time, a bias in the expected value of DIS_2 is + 1.4% (4080 ppm instead of 4028 ppm) with a relative expanded uncertainty of ±5.4%. The sensitivity of the expanded uncertainty of DIS_1 (resp. DIS_2) versus the expanded uncertainty in PM characterization is 115×10^3 ppm/T (resp. 15×10^3 ppm/T).

The uncertainty in the actual orientation of the PMs, caused by the mechanical tolerances of the structure, introduces a smaller bias effect in the expected value of DIS_1 (23 370 ppm against 23 200 ppm, that is + 0.7%) with an expanded uncertainty of ±3.2% (with a 95% coverage interval). The bias in the expected value of DIS_2 is + 0.1% (4032 ppm instead of 4028 ppm) with an expanded uncertainty of ±2.2%. The sensitivity of the expanded uncertainty of DIS_1 (resp. DIS_2) versus the maximum deviation of angle orientation is 83.4×10^3 ppm/rad (resp. 9.92×10^3 ppm/rad).

Weaker bias effects are found on the expected value of DIS_1 and DIS_2 due to variability in the PM samples (around + 0.4%) and PM positioning (less than 0.3%). The sensitivity of the expanded uncertainty of DIS_1 (resp. DIS_2) versus the expanded uncertainty in PM characterization is 54×10^3 ppm/T (resp. 5.6×10^3 ppm/T), while the sensitivity of the expanded uncertainty of DIS_1 (resp. DIS_2) versus the maximum deviation of PM positioning is 3.4×10^6 ppm/m (resp. 0.33×10^6 ppm/m).

The combination of all the stochastic effects causes an increase in the expected DIS_1 value of + 1.7% (23 600 ppm instead of 23 200 ppm) with an expanded uncertainty of ±8.6% (95% coverage interval). The bias in the expected value of DIS_2 is + 1.7% (4100 ppm instead of 4028 ppm) with an expanded uncertainty of ±6.5%.

A good agreement is found between measurement and corrected modeling results, both for the B_0 field value and its homogeneity in the DSV. The 95% coverage interval of the measured B_0 field average is (48.048/48.064) mT, while the model gives (47.45/48.55) mT. For DIS_1, the coverage intervals for the experiment and the model are (23 300/25 900) ppm and (21 600/25 600) ppm, respectively. For DIS_2, the coverage intervals for the experiment and the model are (3100/5700) ppm and (3800/4400) ppm, respectively. A superposition of the coverage intervals is always found, demonstrating consistency between measurements and modeling predictions.

It should be noted that this study did not analyze the effects of the magnetic field's temporal stability. This is also crucial for practical applications involving long-term data acquisition, as it ensures the reliability of the data and requires specific, detailed analysis.

VII. Conclusion

This study used a reference magnet array design to investigate the main factors responsible for discrepancies between the expected and measured performances.

Understanding how choices made during magnet construction impact the magnet performance, potentially helps in achieving more effective and reliable designs. Furthermore, analyzing sensitivity to stochastic effects of variability highlights the importance of optimizing the magnet using a configuration that is more robust against variations in the input data. All of this has a direct effect on the performance of the scanner in terms of image quality.

Finally, the results of the analysis can be leveraged to select the manufacturing tolerances in a more informed manner and, consequently, eliminate or at least simplify the shimming phase. In the latter case, the results may pave the way for an "informed shimming," whereby the variability in the positioning and orientation of additional magnets can be substantially reduced.

In both cases, reducing production costs is feasible and would be relevant and useful to the wider portable MRI community.

Datasets

All datasets are available at the Zenodo repository https://doi.org/10.5281/zenodo.15879992

Appendix A

The measurement models of parameters DIS_1 and DIS_2 are

$$\mathrm{DIS}_1 = \frac{B_{x\max} - B_{x\min}}{B_{x\mathrm{mean}}} \cdot C_{\mathrm{off1}} \tag{A1}$$

$$\mathrm{DIS}_2 = \sqrt{\frac{1}{N}\sum_i (B_{xi} - B_{x\mathrm{mean}})^2} \cdot C_{\mathrm{off2}} \tag{A2}$$

where

B_x x-component of the magnetic field B. The subscripts max, min, and mean indicate the maximum, minimum, and the mean measured values. Its uncertainty value is computed below;

$C_{\mathrm{off},1}$ and $C_{\mathrm{off},2}$ two unitary coefficients whose uncertainty takes into account the influence of the magnet array position with respect to the origin of the measurement system. The array position in the measurement system was uncertain up to ± 2 mm along each Cartesian axis with a uniform distribution. Simulations showed that moving the DSV according to these limits causes the values of the DIS_1 and DIS_2 to change by a maximum of 4.8% and 1%, respectively. This resulted in a standard relative uncertainty equal to 14 000 and 3000 ppm for the DIS_1 and DIS_2 values, respectively;

N total number of measured values and equals 4224.

The measurement model for the x-component of the magnetic flux density, B_x, is

$$B_x = B_{x,\mathrm{meas}} + C_{\mathrm{noise}} + C_{\mathrm{res}} + C_{\mathrm{avg}} + C_{\mathrm{pos}} + C_{\mathrm{temp}} \tag{A3}$$

where

$B_{x,\mathrm{meas}}$ measured value of the x-component of the magnetic flux density in a specific spatial point inside the DSV. Its relative uncertainty was determined by calibration with a reference NRM probe and equals 20 ppm;

C_{noise} zero average coefficient whose uncertainty accounts for the measurement noise;

C_{res} zero average coefficient whose uncertainty accounts for the instrument's digital resolution;

C_{avg} zero average coefficient whose uncertainty accounts for the dimension of the sensor. Its uncertainty was obtained from the maximum sensor linear dimension (100 μm) multiplied by the maximum B_x gradient within the DSV and assessed through simulations (13.56 mT/m);

C_{pos} zero average coefficient whose uncertainty accounts for the uncertain position of the magnetic field probe, both due to the automatic movement system and the mechanical tolerance of the 3-D printed holder. The centering of the magnet array within the area scanned by the movement system has been measured with a resolution of ± 0.5 mm, and the tolerance of the probe holder is ± 0.5 mm as well. By combining these contributions, the C_{pos} uncertainty was obtained by multiplication with the maximum B_{x} gradient within the DSV assessed through simulations (13.56 mT/m);

C_{temp} zero average coefficient whose uncertainty accounts for the temperature variation during the measurements. The measurement temperature equals (23.7 $\pm$ 0.32) °C. Equation (1a) and (1b) are allowed to compute the uncertainty associated with the coefficient C_{temp}.

Table III collects all the uncertainty contributions together with their standard and expanded uncertainty values. The last two rows of the table report the uncertainty values linearly propagated to the DIS_1 and DIS_2 measured values. All contributions have been propagated in accordance with [53].

Appendix B

To extend the dipole modeling approach to account for magnet interactions and nonlinearities, the "working point" of each magnet has to be computed according to its linear or nonlinear magnetic characteristics. The total magnetic field inside magnet i ($H_v^{(i)}$) is given by the sum of the "internal" magnetic field ($H_{v,\mathrm{int}}^{(i)}$), represented by the demagnetizing factor $\aleph$

$$H_{v,\mathrm{int}} = -\frac{\aleph}{\mu_0} \cdot J_v \tag{B1}$$

and the superposition of the "external" contributions ($H_{v,\mathrm{ext}}$) coming from all other magnets, evaluated in the barycenter of magnet i by using (5). The demagnetizing factor is given by

$$\aleph = \frac{L_u L_w}{L_u L_v + L_u L_w + L_v L_w}. \tag{B2}$$

Therefore, for the generic magnet i, we can write the total magnetic field as

$$H_v^{(i)} = -\frac{\aleph^{(i)}}{\mu_0} J_v^{(i)} + \left(\sum\nolimits_{p\neq i}^{P} J_v^{(p)} \boldsymbol{F}_{p,i}\right) \cdot \boldsymbol{v}^{(i)} \tag{B3}$$

where $\boldsymbol{v}^{(i)}$ is the unit vector of the local axis v of magnet i, $F_{p,i}$ is the coefficient of interaction between magnet i and the generic magnet p, being P the total number of magnets in the array. Note that, in (B3), the field contribution of the generic magnet p is projected along the axis of magnetization $v^{(i)}$ of magnet i. Introducing the magnetic characteristic, $J_v^{(i)}$ is expressed as

$$J_v^{(i)} = \mu_0 \mu_M H_v^{(i)} + J_r^{(i)} \ (\text{linear} H - J \text{characteristic}) \tag{B4a}$$

$$J_v^{(i)} = g\left(H_v^{(i)}\right) + J_r^{(i)} \ (\text{nonlinear} H - J \text{characteristic}) \tag{B4b}$$

where g is the monotonic function representing the H–J magnetic characteristic.

Making reference to the nonlinear case, (B4b) can be solved using the fixed point (FP) technique [52], introducing an arbitrary linear term (slope μ_{FP}) plus a residual R to be iteratively computed

$$J_v^{(i)} = g\left(H_v^{(i)}\right) + J_r^{(i)} = \mu_{\text{FP}} H_v^{(i)} + R^{(i)} + J_r^{(i)}. \tag{B5}$$

By elaborating on (B3) and considering (B5), we can derive the final equation for the generic magnet i

$$\begin{aligned} &- \aleph^{(i)} \mu_{\text{FP}} H_v^{(i)} - \mu_0 H_v^{(i)} + \mu_0 \mu_{\text{FP}} \sum_{p \neq i}^{P} \left(\boldsymbol{F}_{pi} \cdot \boldsymbol{v}^{(i)}\right) H_v^{(p)} \\ &= \aleph^{(i)} J_r^{(i)} - \mu_0 \sum_{p \neq i}^{P} \left(\boldsymbol{F}_{pi} \cdot \boldsymbol{v}^{(i)}\right) J_r^{(p)} \\ &\quad + \aleph^{(i)} R^{(i)} - \mu_0 \sum_{p \neq i}^{P} \left(\boldsymbol{F}_{p,i} \cdot \boldsymbol{v}^{(i)}\right) R^{(p)} \end{aligned} \tag{B6}$$

which simplifies to the linear model when $\mu_{\text{FP}} = \mu_0 \mu_M$ and $R = 0$.

By writing (B6) for all magnets ($i = 1,..., P$), we obtain the final system of equations

$$\boldsymbol{M}\boldsymbol{H}_v = \boldsymbol{T}_J + \boldsymbol{T}_R \tag{B7}$$

where $\boldsymbol{H}_v$ is the vector containing the unknown values of the main components (local v-axis) of the magnetic field inside each magnet, M is a matrix accounting for the PM shape and interaction between PMs, and $\boldsymbol{T}_J$, $\boldsymbol{T}_R$ are known terms, including magnetization and FP residuals, respectively; the latter being zero for linear magnetic characteristics. The system of equations (B7) can be solved iteratively, starting from an arbitrary initial value of $\boldsymbol{T}_R$ (usually zero), until a given convergence tolerance is reached. At each FP iteration, the residual values $R^{(i)}$ are updated as follows:

$$R^{(i)} = g\left(H_v^{(i)}\right) - \mu_{\text{FP}} H_v^{(i)}. \tag{B8}$$

Usually, some tens of iterations (<50) are sufficient to reach a relative convergence tolerance lower than 10^{-7}.

Finally, in Fig. 9, a simple diagram schematically showing the different ways of modeling the PMs array is shown.

Acknowledgment

The authors thank Dr. Lukas Winter and Dr. Martin Häuer from PTB for providing the mechanical frame of the magnet. They also thank Dr. Tom O'Reilly for sharing all the data necessary for simulating the magnetic field distribution generated by the array. The study was performed in the framework of the 22HLT02 A4IM project. The project 22HLT02 A4IM has received funding from the European Partnership on Metrology, co-financed by the European Union's Horizon Europe Research and Innovation Programme and by the Participating States.

References

[1] J. Hennig, "An evolution of low-field strength MRI," *Magn. Reson. Mater. Phys., Biol. Med.*, vol. 36, no. 3, pp. 335–346, Jun. 2023, doi: 10.1007/s10334-023-01104-z.

[2] T. C. Arnold, C. W. Freeman, B. Litt, and J. M. Stein, "Low-field MRI: Clinical promise and challenges," *J. Magn. Reson. Imag.*, vol. 57, no. 1, pp. 25–44, Jan. 2023, doi: 10.1002/jmri.28408.

[3] E. Anoardo and G. G. Rodriguez, "New challenges and opportunities for low-field MRI," *J. Magn. Reson. Open*, vols. 14–15, Jun. 2023, Art. no. 100086, doi: 10.1016/j.jmro.2022.100086.

[4] A. Altaf et al., "Applications, limitations and advancements of ultra-low-field magnetic resonance imaging: A scoping review," *Surgical Neurol. Int.*, vol. 15, p. 218, Jun. 2024, doi: 10.25259/sni_162_2024.

[5] B. Mašková, M. Rožánek, O. Gajdoš, E. Karnoub, V. Kamenský, and G. Donin, "Assessment of the diagnostic efficacy of low-field magnetic resonance imaging: A systematic review," *Diagnostics*, vol. 14, no. 14, p. 1564, Jul. 2024, doi: 10.3390/diagnostics14141564.

[6] M. Hori, A. Hagiwara, M. Goto, A. Wada, and S. Aoki, "Low-field magnetic resonance imaging: Its history and renaissance," *Investigative Radiol.*, vol. 56, no. 11, pp. 669–679, 2021, doi: 10.1097/rli.0000000000000810.

[7] A. Samardzija et al., "Low-field, low-cost, point-of-care magnetic resonance imaging," *Annu Rev Biomed Eng.*, vol. 26, no. 1, pp. 67–91, 2024, doi: 10.1146/annurev-bioeng-110122-022903.

[8] M. Sarracanie and N. Salameh, "Low-field MRI: How low can we go? A fresh view on an old debate," *Frontiers Phys.*, vol. 8, pp. 1–14, Jun. 2020, Art. no. 172, doi: 10.3389/fphy.2020.00172.

[9] A. E. Campbell-Washburn et al., "Low-field MRI: A report on the 2022 ISMRM workshop," *Magn. Reson. Med.*, vol. 90, no. 4, pp. 1682–1694, Oct. 2023, doi: 10.1002/mrm.29743.

[10] ISMRM Annual Meeting, London,. *High-Field to Very- & Ultra-Low-Field MRI: What's Different*. [Online]. Available: https://www.ismrm.org/21/program-files/WE-24.htm

[11] Y. Liu et al., "A low-cost and shielding-free ultra-low-field brain MRI scanner," *Nature Commun.*, vol. 12, no. 1, p. 7238, Dec. 2021, doi: 10.1038/s41467-021-27317-1.

[12] W. T. Kimberly et al., "Brain imaging with portable low-field MRI," *Nature Rev. Bioeng.*, vol. 1, no. 9, pp. 617–630, Jul. 2023, doi: 10.1038/s44222-023-00086-w.

[13] A. J. Sorby-Adams et al., "Portable, low-field magnetic resonance imaging for evaluation of Alzheimer's disease," *Nature Commun.*, vol. 15, Dec. 2024, Art. no. 10488, doi: 10.1038/s41467-024-54972-x.

[14] X. Kong et al., "A low-cost portable 50 mT MRI scanner for dental imaging," *IEEE Trans. Instrum. Meas.*, vol. 73, pp. 1–11, 2024, doi: 10.1109/TIM.2023.3329089.

[15] S. C. L. Deoni et al., "Development of a mobile low-field MRI scanner," *Sci. Rep.*, vol. 12, Apr. 2022, Art. no. 5690, doi: 10.1038/s41598-022-09760-2.

[16] C. Z. Cooley et al., "Two-dimensional imaging in a lightweight portable MRI scanner without gradient coils," *Magn. Reson. Med.*, vol. 73, no. 2, pp. 872–883, Feb. 2015, doi: 10.1002/mrm.25147.

[17] G. Frija, D. H. Salama, M. G. Kawooya, and B. Allen, "A paradigm shift in point-of-care imaging in low-income and middle-income countries," *eClinicalMedicine*, vol. 62, Aug. 2023, Art. no. 102114, doi: 10.1016/j.eclinm.2023.102114.

[18] C. Z. Cooley et al., "A portable scanner for magnetic resonance imaging of the brain," *Nature Biomed. Eng.*, vol. 5, no. 3, pp. 229–239, Nov. 2020, doi: 10.1038/s41551-020-00641-5.

[19] Z. H. Ren, S. Obruchkov, D. W. Lu, R. Dykstra, and S. Y. Huang, "A low-field portable magnetic resonance imaging system for head imaging," in *Proc. Prog. Electromagn. Res. Symp. Fall (PIERS-FALL)*, Singapore, Nov. 2017, pp. 3042–3044.

[20] T. O'Reilly, W. M. Teeuwisse, D. de Gans, K. Koolstra, and A. G. Webb, "In vivo 3D brain and extremity MRI at 50 mT using a permanent magnet Halbach array," *Magn. Reson. Med.*, vol. 85, no. 1, pp. 495–505, Jan. 2021, doi: 10.1002/mrm.28396.

[21] D. Schote et al., "Nexus: A versatile console for advanced low-field MRI," *Magn. Reson. Med.*, vol. 93, no. 5, pp. 2224–2238, May 2025, doi: 10.1002/mrm.30406.

[22] Y. Zhao et al., "Whole-body magnetic resonance imaging at 0.05 Tesla," *Science*, vol. 384, no. 6696, pp. 1–12, May 2024, doi: 10.1126/science.adm7168.

[23] T. O'Reilly, W. M. Teeuwisse, and A. G. Webb, "Three-dimensional MRI in a homogenous 27 cm diameter bore Halbach array magnet," *J. Magn. Reson.*, vol. 307, Oct. 2019, Art. no. 106578, doi: 10.1016/j.jmr.2019.106578.

[24] P. Blümler and H. Soltner, "Practical concepts for design, construction and application of Halbach magnets in magnetic resonance," *Appl. Magn. Reson.*, vol. 54, nos. 11–12, pp. 1701–1739, Dec. 2023, doi: 10.1007/s00723-023-01602-2.

[25] C. W. Windt, H. Soltner, D. V. Dusschoten, and P. Blümler, "A portable Halbach magnet that can be opened and closed without force: The NMR-CUFF," *J. Magn. Reson.*, vol. 208, no. 1, pp. 27–33, Jan. 2011, doi: 10.1016/j.jmr.2010.09.020.

[26] M. C. D. Tayler and D. Sakellariou, "Low-cost, pseudo-Halbach dipole magnets for NMR," *J. Magn. Reson.*, vol. 277, pp. 143–148, Apr. 2017, doi: 10.1016/j.jmr.2017.03.001.

[27] T. O'Reilly, W. Teeuwisse, and A. Webb, "A new approach to shimming Halbach arrays using higher order Halbach array inserts," *Int. Soc. Magn. Reson. Med.*, vol. 30, Jan. 2022, doi: 10.58530/2022/0063.

[28] K. Koolstra, T. O'Reilly, P. Börnert, and A. Webb, "Image distortion correction for MRI in low field permanent magnet systems with strong B0 inhomogeneity and gradient field nonlinearities," *Magn. Reson. Mater. Phys., Biol. Med.*, vol. 34, no. 4, pp. 631–642, Aug. 2021, doi: 10.1007/s10334-021-00907-2.

[29] J. Wang et al., "Design and shimming method of low length-to-interdiameter ratio Halbach magnet," *IEEE Trans. Instrum. Meas.*, vol. 71, pp. 1–10, 2022, doi: 10.1109/TIM.2022.3199233.

[30] A. Bogaychuk and E. Ivshin, "Improving the homogeneity of Halbach arrays by optimizing magnet combinations using a genetic algorithm," *Rev. Sci. Instrum.*, vol. 95, no. 5, May 2024, Art. no. 055107, doi: 10.1063/5.0191486.

[31] C. Z. Cooley et al., "Design of sparse Halbach magnet arrays for portable MRI using a genetic algorithm," *IEEE Trans. Magn.*, vol. 54, no. 1, pp. 1–12, Jan. 2018, doi: 10.1109/TMAG.2017.2751001.

[32] T.-O. Liang, Y. H. Koh, T. Qiu, E. Li, W. Yu, and S. Y. Huang, "High-performance permanent magnet array design by a fast genetic algorithm (GA)-based optimization for low-field portable MRI," *J. Magn. Reson.*, vol. 345, Dec. 2022, Art. no. 107309, doi: 10.1016/j.jmr.2022.107309.

[33] L. Xuan, Y. Zhang, J. Wu, Y. He, F. Chen, and Z. Xu, "Geometry-based shim coil design applied on an ultralow-field MRI system," *IEEE Trans. Instrum. Meas.*, vol. 72, pp. 1–11, 2023, doi: 10.1109/TIM.2023.3311060.

[34] Y. Shang, G. L. Simegn, K. Gillen, H.-J. Yang, and H. Han, "Advancements in MR hardware systems and magnetic field control: B0 shimming, RF coils, and gradient techniques for enhancing magnetic resonance imaging and spectroscopy," *Psychoradiology*, vol. 4, Feb. 2024, Art. no. kkae013, doi: 10.1093/psyrad/kkae013.

[35] C. Wan, W. He, and Z. Xu, "A flexible quadrature coil for very-low-field (50.4 mT) knee magnetic resonance imaging," *IEEE Trans. Instrum. Meas.*, vol. 72, pp. 1–12, 2023, doi: 10.1109/TIM.2023.3311068.

[36] X. Kong et al., "Gradient coil design method specifically for permanent-magnet-type low field portable MRI brain scanner," *IEEE Trans. Instrum. Meas.*, vol. 72, pp. 1–12, 2023, doi: 10.1109/TIM.2022.3225042.

[37] V. Lau et al., "Pushing the limits of low-cost ultra-low-field MRI by dual-acquisition deep learning 3D superresolution," *Magn. Reson. Med.*, vol. 90, no. 2, pp. 400–416, Aug. 2023, doi: 10.1002/mrm.29642.

[38] (Jul. 2025). *The Open Source Imaging Initiative (OSI^2)*. [Online]. Available: https://www.opensourceimaging.org/

[39] G. Mörée, J. Sjölund, and M. Leijon, "A review of permanent magnet models used for designing electrical machines," *IEEE Trans. Magn.*, vol. 58, no. 11, pp. 1–19, Nov. 2022, doi: 10.1109/TMAG.2022.3200150.

[40] (Jul. 2025). *Open Source Imaging Initiative (OSI^2)*. OSII 30 cm Halbach Magnet. [Online]. Available: https://gitlab.com/osii/magnet/30cm-halbach-magnet/-/tree/releases/2.1?ref_type=heads

[41] H. Raich and P. Blümler, "Design and construction of a dipolar Halbach array with a homogeneous field from identical bar magnets: NMR mandhalas," *Concepts Magn. Reson. B, Magn. Reson. Eng.*, vol. 23B, no. 1, pp. 16–25, Oct. 2004.

[42] (Jul. 2025). *Open Source Imaging Initiative (OSI^2)*. Assembly Guide. [Online]. Available: https://gitlab.com/osii/magnet/30cm-halbach-magnet/-/blob/main/doc/assembly-guide.md?ref_type=heads

[43] U. Zanovello, V. Basso, and L. Winter, "A low-cost and open-source magnet test station to improve the assembly process of low-field scanner magnets," in *Proc. ISMRM Annu. Meeting*, Singapore, 2024.

[44] OSII. (Jul. 2025). *Magnet Test Station*. Accessed: Dec. 4, 2025. [Online]. Available: https://gitlab.com/osii/tools/MagnetTestStation

[45] Dassault Systems. (Jul. 2025). *CST Studio Suite*. [Online]. Available: https://www.3ds.com/products/simulia/cst-studio-suite

[46] R. Engel-Herbert and T. Hesjedal, "Calculation of the magnetic stray field of a uniaxial magnetic domain," *J. Appl. Phys.*, vol. 97, no. 7, Apr. 2005, Art. no. 074504.

[47] INRiM. (Jul. 2025). *Array_Dipoles*. [Online]. Available: https://github.com/orianobottauscio/Array_Dipoles/tree/main

[48] Methods of Measurement of the Magnetic Dipole Moment of a Ferromagnetic Material Specimen by the Withdrawal or Rotation Method, Standard IEC 60404-14, IEC Central Office, Geneva, Switzerland, 2002.

[49] BIPM-KCDB,. *Code: INRIM/249, CMC-ID: EURAMET-EM-IT-00000EJC-1*. [Online]. Available: https://www.bipm.org/kcdb/

[50] (Jul. 2025). *Stanford Magnets*. Accessed: Dec. 4, 2025. [Online]. Available: https://www.stanfordmagnets.com/tolerance-limits-for-different-magnet-processes.html

[51] Open Source Imaging Initiative (OSI2). (Jul. 2025). *Manufacturing Guide*. [Online]. Available: https://gitlab.com/osii/magnet/30cm-halbach-magnet/-/blob/main/doc/manufacturing-guide.md?ref_type=heads

[52] O. Bottauscio, D. Chiarabaglio, M. Chiampi, and M. Repetto, "A hysteretic periodic magnetic field solution using Preisach model and fixed point technique," *IEEE Trans. Magn.*, vol. 31, no. 6, pp. 3548–3550, Aug. 1995, doi: 10.1109/20.489565.

[53] *Evaluation of Measurement Data Guide to the Expression of Uncertainty in Measurement*, JCGM 100:2008(E), 2008, doi: 10.59161/JCGM100-2008E.

Umberto Zanovello was born in Turin, Italy, in 1988. He received the B.S. and M.S. degrees in electrical engineering and the Ph.D. degree in electrical, electronics and communications engineering from the Politecnico di Torino, Turin, in 2011, 2014, and 2019, respectively.

He has been a permanent Researcher with the Istituto Nazionale di Ricerca Metrologica (INRiM), Turin, since 2021. His research interests include MRI safety and hardware design, with a particular focus on low-field MRI and radio frequency coils.

Alessandro Arduino received the B.Sc. degree in mathematics for engineering sciences, the M.Sc. degree in mathematical engineering, and the Ph.D. degree in electrical, electronics, and communications engineering from the Politecnico di Torino, Turin, Italy, in 2012, 2014, and 2018, respectively.

Since 2018, he has been with the Istituto Nazionale di Ricerca Metrologica, Turin. He is the Maintainer of EPTlib, an open-source C++ library of magnetic resonance-based electric properties tomography methods. His research interests include mathematical and numerical modeling of electromagnetism applied to biomedical engineering and inverse problems.

3.5pt Vittorio Basso has currently a Research Scientist at the Istituto Nazionale di Ricerca Metrologica, Turin, Italy, since 1995. He is responsible for the INRIM Magnetic Measurement Laboratory, Turin. He is the co-author of 160 peer-reviewed publications. His research interests include the physics of magnetic materials and spintronics.

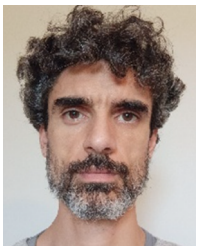

Luca Zilberti was born in Vercelli, Italy, in 1982. He received the B.Sc., M.Sc., and Ph.D. degrees in electrical engineering from the Politecnico di Torino, Turin, Italy, in 2004, 2006, and 2010, respectively.

In 2010, he joined the Istituto Nazionale di Ricerca Metrologica, Turin, where he is currently a Senior Researcher. In 2022, he got the national qualification as a Full Professor for electrical engineering. His research interests include the development of computational methods for electromagnetic dosimetry and biomedical applications of electromagnetic fields.

Dr. Zilberti also serves on the governing committee of the study group on the MR Safety of the International Society for Magnetic Resonance in Medicine (ISMRM). He coordinated the European EMPIR Project 18HLT05 "Quantitative MR-Based Imaging Of Physical Biomarkers" from 2019 to 2022 and currently coordinates European EPM Project 24DIT01 APULEIO "Trustworthy and Quality-Assured Quantitative Magnetic Resonance Imaging" from 2025 to 2028. In 2016, he was a recipient of the Young Scientist Award from the International Commission on Non-Ionizing Radiation Protection (ICNIRP).

Alessandro Sola was born in Turin, Italy, in 1984. He received the B.Sc. and M.Sc. degrees in physics from the University of Turin, Turin, and the Ph.D. degree in physics from Politecnico di Torino, Turin, in 2014.

In 2014, he joined the Istituto Nazionale di Ricerca Metrologica (INRIM), Turin, as a Post-Doctoral Researcher and since 2020 as a permanent Researcher. He leads the laboratory for the characterization of hard magnetic materials at INRIM, and his research interests include magnetic materials, spin caloritronics, and the transverse thermoelectric effect.

Andrea Agosto was born in Carmagnola, Italy, in 1981. He received the High School Diploma degree in electronics and telecommunications from the Istituto Tecnico Industriale Statale Pininfarina, Moncalieri (TO), Italy, in 2000.

He has been a Technical Collaborator and a Software Developer at the Istituto Nazionale di Ricerca Metrologica (INRIM), Turin, Italy, since 2001, and he is currently the Laboratory Manager and an Activity Manager for calibration of ac magnetic sources and meters. He has been and continues to be Quality Assistant of the Advanced Materials Metrology and Life Science Division, and is responsible for quality implementation and maintenance/improvement of the INRiM QMS for the ac magnetic measurement laboratories of the ML Division. He co-drafts and co-revises technical procedures for performing calibrations, tests, and measurements.

Luca Toso was born in Turin, Italy, in 1973. He received the M.Sc. degree in electronics engineering from the Politecnico di Torino, Turin, Italy, in 1992.

He has been a Technical Collaborator at the Istituto Nazionale di Ricerca Metrologica (INRIM), Turin, since 1994, where he is currently the Laboratory Manager and the Activity Manager for calibration of analog/digital instruments for measuring static magnetic quantities. He has been and continues to be responsible for quality implementation and maintenance/improvement of the INRIM QMS for the dc magnetic measurement laboratories of the ML Division. He co-drafts and co-revises technical procedures for performing calibrations, tests, and measurements.

Oriano Bottauscio was born in Turin, Italy, in 1961. He received the M.Sc. degree in electrical engineering from the Politecnico di Torino, Turin, in 1985.

In 1987, he joined the Istituto Nazionale di Ricerca Metrologica (INRiM), formerly Istituto Elettrotecnico Nazionale Galileo Ferraris, Turin, and got the level of Research Director in 2012. In the same year, he received the qualification as a Full Professor of electrotechnics. In 2015, he was a Member of the Board of Professors of the Ph.D. course in metrology at the Politecnico di Torino. Since 2018, he has been the Deputy Coordinator of INRiM. He is the author of more than 250 journal articles, with around 2700 citations (H-index 27). His research interests include computational electromagnetism for biomedical applications, with a main emphasis on MRI safety and medical devices. He is the INRiM contact person in the EURAMET Technical Committee of Interdisciplinary Metrology.

Open Access funding provided by 'Istituto Nazionale di Ricerca Metrologica - INRiM' within the CRUI CARE Agreement